A VISION-BASED NAVIGATION ALGORITHM FOR AUTONOMOUS DEEP-SPACE CRUISE

E. Andreis[1*], P. Panicucci[1], V. Franzese[1] and F. Topputo[1]; [1]Department of Aerospace Science and Technology, Politecnico di Milano, Milano, Italy; [*] eleonora.andreis@polimi.it.

Abstract. *A new era of space exploitation is fast approaching. An exponential number of CubeSats, shoeboxed spacecraft, will be launched into space, owing to their low cost compared to traditional probes. At the current pace, piloting CubeSats from the ground with standard radiometric tracking will become unsustainable. This work tackles the problem from the navigation point of view by developing a fully autonomous vision-based navigation algorithm suited to deep-space miniaturized platforms. An extended Kalman filter featuring planet position extraction from deep-space images is exploited to determine the probe trajectory onboard. Preliminary results show that accuracy of about 1000 km and 0.5 m/s for the position and velocity components can be reached in deep space.*

Introduction. The space economy is booming. A significant role is played by deep space exploration, whose growth is driven by the increasing number of missions planned by space agencies and by the advent of deep-space CubeSats. These miniaturized probes have triggered a revolution in the way satellites have been launched into space, owing to their low cost and reduced development time compared to traditional spacecraft.[1] Under the propulsive momentum of the new space economy, several deep-space CubeSats applications are foreseen.[2,3] Yet, their growth is unsustainable with current practice.[4]

Operating a deep-space probe involves determining its position, planning its trajectory, and controlling its motion. Currently, the probe position is estimated by exchanging a two-way signal between ground stations and spacecraft.[5] Yet, ground control requires large teams of engineers, takes a large share of the space mission cost, and has a limited number of communication slots which restricts the number of manageable probes. In other terms, the escalation of miniaturized satellites into deep space will soon lead to the saturation of ground-based facilities, and human-in-the-loop navigation for interplanetary missions will quickly become unsustainable.[4]

Autonomous navigation alternatives could represent a solution to this problem, such as autonomous X-ray pulsar-based,[6] autonomous radio-based,[7] and vision-based navigation (VBN). Among these approaches, VBN is a cheap and fully ground-independent solution, which enables interplanetary CubeSats to determine their position by observing the movement of celestial bodies on images taken by optical sensors, such as cameras or star trackers.

In deep space, Solar System bodies, e.g., planets and asteroids, are unresolved, meaning their light falls in one pixel only of the image.[8] In this framework, the celestial body Line-of-Sight (LoS) direction, extracted from the image, can be exploited as information to navigate the spacecraft.[9,10]

Moreover, to embrace the low-budget paradigm, the optical camera placed onboard a CubeSat is usually cheap and of limited performance, yielding an arduous detection of fainter celestial objects, like asteroids, on images.[11] Thus, when a commercial-off-the-shelf (COTS) miniaturized camera is used, planet LoS directions only can be exploited as observation for VBN of interplanetary CubeSats. First, this information is extracted from the image through image processing (IP) algorithms and, then, it is processed by orbit determination (OD) filters, which output the spacecraft state, i.e., position and velocity.

In the framework of autonomous interplanetary navigation, on one side, the state-of-the-art focuses mainly on implementing onboard orbit determination algorithms to estimate the probe state.[12–14] On the other side, while a detailed pipeline for Image Processing (IP) at mid- and close-range is available,[15–17] few are the works developing an IP pipeline for the extraction of the planet LoS direction,[18,19] and even fewer are the ones presenting a complete navigation cycle. In this context, the present work, framed within the ERC-funded EXTREMA (Engineering Extremely Rare Events in Astrodynamics for Deep-Space Mission in Autonomy) project,[20] wants to propose an exhaustive autonomous vision-based navigation algorithm suited for deep-space miniaturized probes. The work combines an image processing (IP) pipeline for the extraction of planet information from the image[18] with an extended Kalman filter (EKF) based on the celestial triangulation approach.[10,14,21] In addition, since in interplanetary space light effects, i.e., light-time and light aberration,[10] become significant due to the consistent velocity of the probe and the enormous distance between the spacecraft and the planet, their action is included in the DART Lab sky simulator,[22] and their corrections are implemented in the navigation filter.

Problem Statement. A probe, whose state is unknown, is on an interplanetary orbit. The kinematic celestial triangulation problem can be exploited to recover the probe position with only the requirement of acquiring two LoS directions associated with different planets simultaneously.[10] The methodology followed by this method is briefly reported hereafter: Let the probe position $\boldsymbol{r}$ be

$$\boldsymbol{r} = \boldsymbol{r}_1 - \rho_1 \hat{\boldsymbol{\rho}}_1 = \boldsymbol{r}_2 - \rho_2 \hat{\boldsymbol{\rho}}_2 \tag{1}$$

where $\boldsymbol{r}_i$ denotes the position of the i-esimal planet with respect to the Sun in an inertial frame, ρ_i the position magnitude of the i-esimal planet with respect to the observer in an inertial frame and $\hat{\boldsymbol{\rho}}_i$ its direction. The planets positions with respect to the Sun in the inertial reference frame are available from their ephemerides, $\hat{\boldsymbol{\rho}}_1$, $\hat{\boldsymbol{\rho}}_2$

can be measured onboard by the imager of the probe, whereas, the ranges ρ_1, ρ_2 are unknown. The scalar multiplication of Eq. (1) by $\hat{\boldsymbol{\rho}}_1$ and $\hat{\boldsymbol{\rho}}_2$ yields to a system of two equations which can be arranged in matrix form as

$$\underbrace{\begin{bmatrix} -1 & \hat{\boldsymbol{\rho}}_1^\top \hat{\boldsymbol{\rho}}_2 \\ -\hat{\boldsymbol{\rho}}_2^\top \hat{\boldsymbol{\rho}}_1 & 1 \end{bmatrix}}_{\boldsymbol{A}} \underbrace{\begin{bmatrix} \rho_1 \\ \rho_2 \end{bmatrix}}_{\boldsymbol{x}} = \underbrace{\begin{bmatrix} \hat{\boldsymbol{\rho}}_1^\top (\boldsymbol{r}_2 - \boldsymbol{r}_1) \\ \hat{\boldsymbol{\rho}}_2^\top (\boldsymbol{r}_2 - \boldsymbol{r}_1) \end{bmatrix}}_{\boldsymbol{b}} \tag{2}$$

described by the linear-algebra problem, $\boldsymbol{A}\boldsymbol{x} = \boldsymbol{b}$. The solution to Eq. 2 is determined as long as $\Delta(\boldsymbol{A}) = -1 + (\hat{\boldsymbol{\rho}}_1^\top \hat{\boldsymbol{\rho}}_2)(\hat{\boldsymbol{\rho}}_2^\top \hat{\boldsymbol{\rho}}_1) \neq 0$, where Δ is the determinant of $\boldsymbol{A}$. The expression of $\Delta(\boldsymbol{A})$ can be also written in the function of γ, which describes the angle between the two planets as seen by the observer (Fig. 1). Since

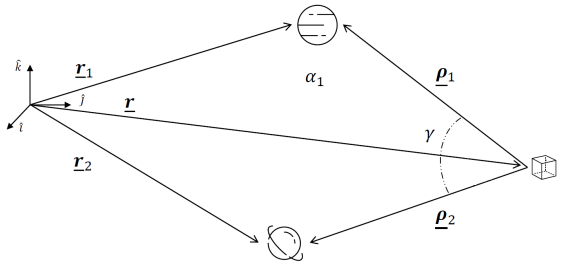

Figure 1. Celestial triangulation problem

$\cos\gamma = \hat{\boldsymbol{\rho}}_1^\top \hat{\boldsymbol{\rho}}_2$, $\Delta(\boldsymbol{A}) = -1 + \cos^2\gamma$. When $\Delta(\boldsymbol{A}) \neq 0$, the problem solution is $\boldsymbol{x} = \boldsymbol{A}^{-1}\boldsymbol{b}$, which plugged into Eq. 1 yields the probe inertial position. Whereas, when $\cos\gamma = \pm 1$, $\boldsymbol{A}$ is singular and the solution is undetermined. This scenario occurs when the probe and the planets are in conjunction or opposition.[23]

Even if the proposed kinematic celestial triangulation method is thought to have a general application, in this work, the CubeSats case study is investigated. Thus, the following constraints are enforced: 1) Only one miniaturized COTS imager (star tracker or navigation camera) is adopted on board, 2) only one beacon at a time is assumed to be observed due to the narrow Field of View (FoV) of the optical sensor, and 3) only planets are tracked because of the limited performances (mainly limit magnitude) of the imager. Therefore, dynamic methods, e.g., Kalman filtering, based on the kinematic celestial triangulation problem and which can work with asynchronous external optical observations need to be adopted for the VBN of interplanetary nanosatellites.

Another critical aspect to consider for deep-space navigation is the action of light effects on the alteration of the external observations adopted to correct the state estimate. In fact, the light-time effect acting on planet observation becomes significant in interplanetary space due to the enormous distance between the spacecraft and the planet. As a result of this effect, the observed projection of the planet position in the sensor frame at the epoch t, when the image is taken, does not correspond to its position projection at that time, but to a previous epoch τ, when the light has been emitted by the planet. The further the planet is from the spacecraft, the more significant the light-time effect is. Instead, the light-aberration effect acquires importance whenever the probe velocity to the target is not negligible, as in the case of a probe moving in the solar system. As the light-time, this effect causes an alteration of the acquired observation, which, in this case, depends on the velocity intensity and direction with respect to the LoS of the observed planet. Corrections of these two effects need to be implemented inside the filter to avoid systematic errors in the probe state estimation.

Image Generation. The generation of the sky-field images input in the VBN filter is performed by adopting an improved version of the DART Lab [1] sky simulator,[14,22] where the light effects are modeled.[10] On one side, the light-time effect is simply included by projecting the planet position at epoch τ instead of at epoch t, when the signal is received by the probe. On the other side, the light-aberration effect is simulated by shifting the LoS directions of the bright objects in the image accordingly to the spacecraft velocity. The procedure illustrated in [10] for the light-aberration correction is exploited, in this work, in the inverse way to model the effect in the sky simulator. The light-time effect shifts only the planet position projection in the image since stars are assumed still in time inside the Solar System. Instead, the light aberration changes the projected position of all centroids found. Furthermore, the sky simulator models also the event of cosmic rays hitting the sensor by randomly turning on some single pixels. Fig. 3a is representative of a sky-field image exploited for deep-space VBN.

Navigation Workflow. In this section, the navigation workflow followed by the VBN filter is illustrated. Over the interplanetary transfer, navigation and state-propagation-only legs are alternated (see Fig. 4). Planets observations are performed in navigation legs only, where two planets are observed asynchronously to triangulate the probe position. Initially, here, the spacecraft tracks the first planet of the pair. Then, it performs a slew maneuver, during which no external observations are acquired, to point to the second planet of the pair, and, eventually, it tracks this latter. During the two acquisition windows, where the spacecraft observes a planet, the VBN filter propagates and corrects the probe state with planet observations. Instead, between two navigation legs and during the slew maneuver, the filter only propagates the probe state as external observations are not acquired. To determine which couple of planets is best to observe in each navigation leg, the optimal planet selection method is adopted,[23] which yields the highest solution accuracy in the estimation of the probe state.[14] At the beginning of each navigation leg, the observability of all the planets is assessed by evaluating their associated Solar Exclusion Angle (SEA) and apparent magnitude. Only those planets whose parameters respect the threshold values im-

[1] `https://dart.polimi.it/`

posed by the optical sensor are considered visible by the camera. Then, the optimal pair is found among the visible planets by minimizing the figure of merit $\mathcal{J}$, which is evaluated for each pair of traceable planets. $\mathcal{J}$ is defined as

$$\mathcal{J} = \sigma_{\text{str}}^2 \frac{1+\cos\gamma^2}{\sin\gamma^4} \boldsymbol{d}^\top \Big(\boldsymbol{L}_i + \boldsymbol{L}_j \Big) \boldsymbol{d} \tag{3}$$

where $\boldsymbol{L}_i = \boldsymbol{I}_{3x3} - \hat{\boldsymbol{\rho}}_i \hat{\boldsymbol{\rho}}_i^\top$ and $\boldsymbol{L}_j = \boldsymbol{I}_{3x3} - \hat{\boldsymbol{\rho}}_j \hat{\boldsymbol{\rho}}_j^\top$; $\hat{\boldsymbol{\rho}}_i$ and $\hat{\boldsymbol{\rho}}_j$ are the unitary LoS vectors to the i-th and j-th planet, respectively. Moreover, σ_{str} is the standard deviation of the LoS angular error from the optical sensor, $\boldsymbol{d} = \boldsymbol{r}_i - \boldsymbol{r}_j$ and $\gamma = \text{acos}(\hat{\boldsymbol{\rho}}_i \hat{\boldsymbol{\rho}}_j)$.

Vision-Based Navigation Filter. A VBN filter embedding asynchronous planets observations in deep space is exploited to recover the probe state. The dynamics and measurement model and the procedure to get the planet observation are described hereunder.

State Dynamics. The process state $\boldsymbol{x}$ is defined as

$$\boldsymbol{x}(t) = [\boldsymbol{r}(t), \boldsymbol{v}(t), \boldsymbol{\eta}(t)]^\top \tag{4}$$

where $\boldsymbol{r}$ and $\boldsymbol{v}$ are the inertial probe position and velocity, respectively, and $\boldsymbol{\eta}$ is a vector of Gauss–Markow (GM) processes accounting for unmodeled terms: a 3-dimensional residual accelerations $\boldsymbol{\eta}_{\text{R}}$ and the stochastic component of the Solar Radiation Pressure (SRP) $\boldsymbol{\eta}_{\text{SRP}}$; that is, $\boldsymbol{\eta} = [\boldsymbol{\eta}_{\text{R}}, \boldsymbol{\eta}_{\text{SRP}}]^\top$.

The process is modeled using the following equation of motion

$$\dot{\boldsymbol{x}}(t) = \boldsymbol{f}(\boldsymbol{x}(t), t) + \boldsymbol{w} \tag{5}$$

where $\boldsymbol{f}$ is the vector field embedding the deterministic part, while $\boldsymbol{w}$ is the process white noise:

$$\boldsymbol{f} = \begin{bmatrix} \boldsymbol{v} \\ \boldsymbol{a}_{\text{Sun}} + \boldsymbol{a}_{\text{SRP}} + \boldsymbol{a}_{\text{pl}_\text{i}} \\ -\xi \boldsymbol{\eta}_{\text{R}} \\ -\xi \boldsymbol{\eta}_{\text{SRP}} \end{bmatrix}$$

where

$$\boldsymbol{a}_{\text{Sun}} = -\mu_{\text{Sun}} \frac{\boldsymbol{r}}{r^3} \tag{6}$$

$$\boldsymbol{a}_{\text{SRP}} = C_{\text{R}} \frac{P_0 R_0^2}{c} \frac{A_{\text{s}}}{m_{\text{s}}} \frac{\boldsymbol{r}}{r^3} \tag{7}$$

$$\boldsymbol{a}_{\text{pl}_\text{i}} = \mu_i \Big(\frac{\boldsymbol{r}_{\text{pl}_\text{i}} - \boldsymbol{r}}{||\boldsymbol{r}_{\text{pl}_\text{i}} - \boldsymbol{r}||^3} - \frac{\boldsymbol{r}_{\text{pl}_\text{i}}}{||\boldsymbol{r}_{\text{pl}_\text{i}}||^3} \Big) \tag{8}$$

$$\boldsymbol{w} = \begin{bmatrix} \boldsymbol{0}_{3x1} \\ \boldsymbol{\eta}_{\text{R}} + \boldsymbol{\eta}_{\text{SRP}} \\ \boldsymbol{w}_{\text{R}} \\ \boldsymbol{w}_{\text{SRP}} \end{bmatrix} \tag{9}$$

The terms that describe the SRP are:[24] C_{R} the coefficient of reflection, P_0 the solar power, R_0 the Sun radius, A_{s} the cross-section area of the probe, and m_{s} its mass. The third-body perturbation of the Earth-Moon barycenter, Mars, and Jupiter is included. In the Langevin equations the coefficient ξ defines the reciprocal of the correlation time, while $\boldsymbol{w}_{\text{R}}$ and $\boldsymbol{w}_{\text{SRP}}$ are the process noises of the GM parameters with σ_{R} and σ_{SRP} standard deviations, respectively.[25] The process noise covariance matrix is $\boldsymbol{Q}$:

$$\boldsymbol{Q} = \text{diag}(\boldsymbol{0}_{3x3}, \boldsymbol{Q}_a, \boldsymbol{Q}_{\text{R}}, \boldsymbol{Q}_{\text{SRP}}) \tag{10}$$

with $\boldsymbol{Q}_{\text{R}} = \sigma_{\text{R}}^2 \boldsymbol{I}_{3x3}$, $\boldsymbol{Q}_{\text{SRP}} = \sigma_{\text{SRP}}^2 \boldsymbol{I}_{3x3}$, and $\boldsymbol{Q}_{\text{a}} = (\boldsymbol{Q}_{\text{R}} + \boldsymbol{Q}_{\text{SRP}})/(2\xi)$.

Observation and Measurement Model. Extraction of the planet observation from the image. The information used for the correction of the state estimate is the position projection of the planet in the sensor frame. A graphic representation of the procedure used to obtain this information is illustrated in Fig. 2. Once the IDs of the optimal pair and its associated

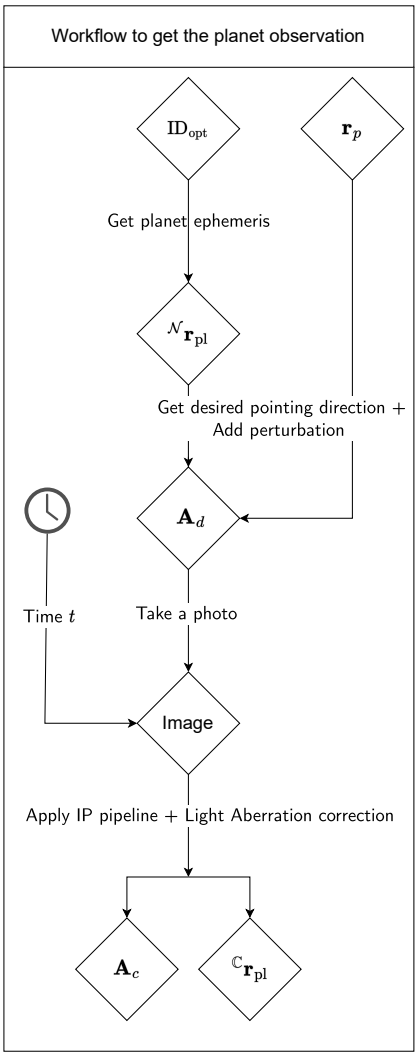

Figure 2. Workflow to get the planet observation

ephemeris $^{\mathcal{N}}\boldsymbol{r}_{\text{pl}}$ in the inertial frame $\mathcal{N}$ are found, and by knowing a previous estimation of the probe position $\boldsymbol{r}_p$, the orientation matrix desired to point to the planet is determined. Since the estimation of the probe position

is known with a certain uncertainty (up to 10^5 km), the beacon projection is not perfectly centered in the image, but still contained in it, which is a sufficient condition to let the IP pipeline[18] extract the planet observation from the image. Moreover, to increase the fidelity of the simulation, a random perturbation is added to the desired pointing direction, and, eventually, an image corresponding to the perturbed probe orientation $\boldsymbol{A}_d$ and observation time t is captured.

To acquire the planet observation from the deep-space image, an IP pipeline suited for the extraction of the position projection of unresolved beacons is adopted. The main steps of this IP pipeline are illustrated in 18. The algorithm performs two tasks:

1. It determines the attitude of the probe through star-pattern recognition by applying the k-vector method.[26] Fig. 3b shows the results of the star identification step.

2. It detects the planet in the image and extracts its position projection by computing the statistical momenta associated with it, which define the Gaussian probability to find the planet in that portion of the image.

Besides these steps, due to the presence of the light-aberration effect, a further procedure needs to be introduced between attitude determination and beacon detection to compensate for it. At this point of the IP pipeline, the light-aberration effect only can be corrected since the planet position projection is still not identified in the image. The compensation is applied to the centroids of the bright objects recognized as stars by the star identification procedure to correct the attitude determination. The decision to not correct the light aberration of the non-stellar objects, among which there is the planet, is to avoid coupling the observation with the state prediction. Indeed, light-aberration compensation requires an estimation of the spacecraft velocity to be implemented as illustrated hereunder.[10] Once an updated value of the probe attitude, i.e., $\boldsymbol{A}_e$, is determined thought the observed stars position projection ${}^{\mathbb{C}}_{h}\boldsymbol{r}_{s_{\text{obs}}}$, the observed LoS direction of the star as seen by the spacecraft in the inertial reference frame ${}^{\mathcal{N}}\boldsymbol{\rho}_{s_{\text{obs}}}$ is computed

$$ {}^{\mathcal{N}}\boldsymbol{\rho}_{s_{\text{obs}}} = (\boldsymbol{K}\boldsymbol{A}_e)^{-1}\,{}^{\mathbb{C}}_{h}\boldsymbol{r}_{s_{\text{obs}}} \tag{11} $$

with $\boldsymbol{K}$ the camera calibration matrix. Moreover, let θ_{obs} be the angle between the observed unitary star LoS direction ${}^{\mathcal{N}}\hat{\boldsymbol{\rho}}_{s_{\text{obs}}}$ and $\hat{\boldsymbol{v}}_p$ the estimated unitary velocity vector of the probe, θ_{obs} can be thus defined as

$$ \tan\theta_{\text{obs}} = \frac{||{}^{\mathcal{N}}\hat{\boldsymbol{\rho}}_{s_{\text{obs}}} \times \hat{\boldsymbol{v}}_p||}{{}^{\mathcal{N}}\hat{\boldsymbol{\rho}}^{\top}_{s_{\text{obs}}}\hat{\boldsymbol{v}}_p} \tag{12} $$

So, the aberration angle ε is

$$ \tan\varepsilon = \frac{(v_p/c)\sin\theta_{\text{obs}}}{1-(v_p/c)\cos\theta_{\text{obs}}} \tag{13} $$

and the correct unitary LoS direction of the star ${}^{\mathcal{N}}\hat{\boldsymbol{\rho}}_{s_{\text{corr}}}$ can be retrieved such that

$$ {}^{\mathcal{N}}\hat{\boldsymbol{\rho}}_{s_{\text{corr}}} = \frac{{}^{\mathcal{N}}\hat{\boldsymbol{\rho}}_{s_{\text{obs}}}\sin\theta_{\text{corr}} - \hat{\boldsymbol{v}}_p\sin\varepsilon}{\sin\theta_{\text{obs}}} \tag{14} $$

with $\theta_{\text{corr}} = \theta_{\text{obs}} + \varepsilon$. Once ${}^{\mathcal{N}}\hat{\boldsymbol{\rho}}_{s_{\text{corr}}}$ is found, Eq. (11) is applied in the direct form and the position projection of the star corrected for the light-aberration effect in the $\mathbb{C}$ reference frame is computed:

$$ {}^{\mathbb{C}}_{h}\boldsymbol{r}_{s_{\text{corr}}} = \boldsymbol{K}\boldsymbol{A}_e\,{}^{\mathcal{N}}\hat{\boldsymbol{\rho}}_{s_{\text{corr}}} \tag{15} $$

At this point, the attitude matrix of the probe is redetermined, i.e., $\boldsymbol{A}_c$, by solving the Wahba problem,[27] in which the corrected star position projections are taken into account. Then, the planet identification step is performed. Once the corrected probe attitude matrix $\boldsymbol{A}_c$, the predicted position of the spacecraft $\boldsymbol{r}_p$, and the ephemeris of the planets are known, the expected position projection of the observed planet in homogeneous coordinates is computed as

$$ {}^{\mathbb{C}}_{h}\boldsymbol{r}_{\text{pl}_0} = \boldsymbol{K}\boldsymbol{A}_c({}^{\mathcal{N}}\boldsymbol{r}_{\text{pl}} - \boldsymbol{r}_p) \tag{16} $$

If ${}^{\mathbb{C}}\boldsymbol{r}_{\text{pl}_0}$ falls inside the image boundaries, its covariance matrix and the associated uncertainty ellipse, which depend on the uncertainties of the spacecraft pose and planet position, can be defined.[18] The covariance matrix of the expected planet position projection represents a portion in the image plane, in which the planet is identified with the highest probability, here considered 3σ. If one or more not-stellar objects are contained in the 3σ uncertainty ellipse, the not-stellar object closest to the expected planet position projection is labeled as the planet projection itself. The closest one is selected because, from a statistical point of view, it is the one with the highest probability of being the projected planet. Therefore, the planet observation adopted to correct the state estimation, i.e., ${}^{\mathbb{C}}\boldsymbol{r}_{\text{pl}}$, is obtained. Figures 3c and 3d graphically show the results of the planet identification step applied to a deep-space image. The green marker ◇ represents the expected position projection of the planet, whose 3σ uncertainty is represented by the green ellipse.

Measurement model. For what concerns the measurement model equation $\boldsymbol{h}$, it is implemented to represent the planet position projection in the sensor frame affected by the light-time and light-aberration effects. Therefore, $\boldsymbol{h}$ describes the planet position projection at epoch τ altered by the light-aberration effect. By including the effects on the measurement model equation and not correcting directly the observed planet projection, the dependency between the observation and the prediction is avoided, and, thus, the correlation of the measurement and process noise error. Eventually, the measurement error covariance matrix $\boldsymbol{R}$ is defined:

$$ \boldsymbol{R} = \sigma^2_{\mathbb{C}_{\boldsymbol{r}_{\text{pl}}}}\boldsymbol{I} \tag{17} $$

where $\sigma^2_{\mathbb{C}_{\boldsymbol{r}_{\text{pl}}}}$ is the standard deviation of the measurement error in pixels.

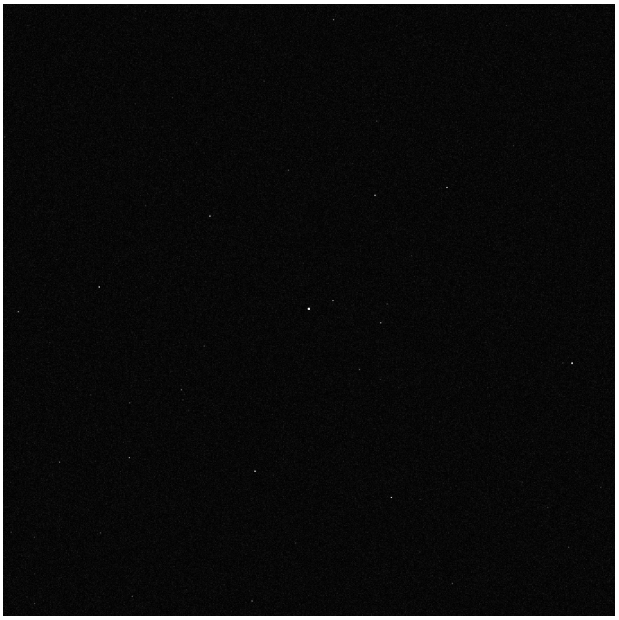

(a) Sky-field image input in the IP pipeline.

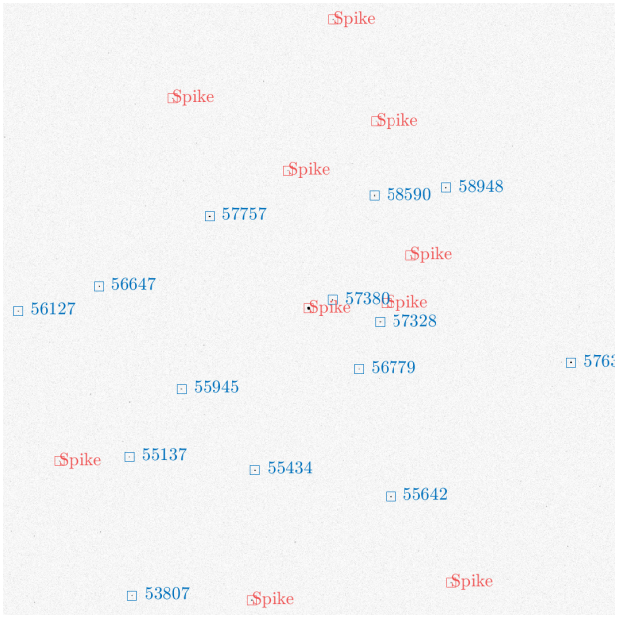

(b) Result of the star identification step applied to Fig. 3a, shown on reverse colors

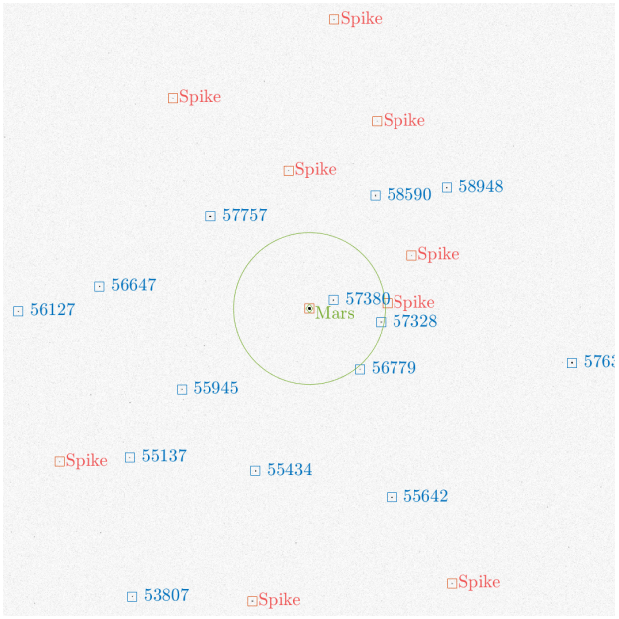

(c) Results of the planet identification step applied to Fig. 3a, shown on reverse colors

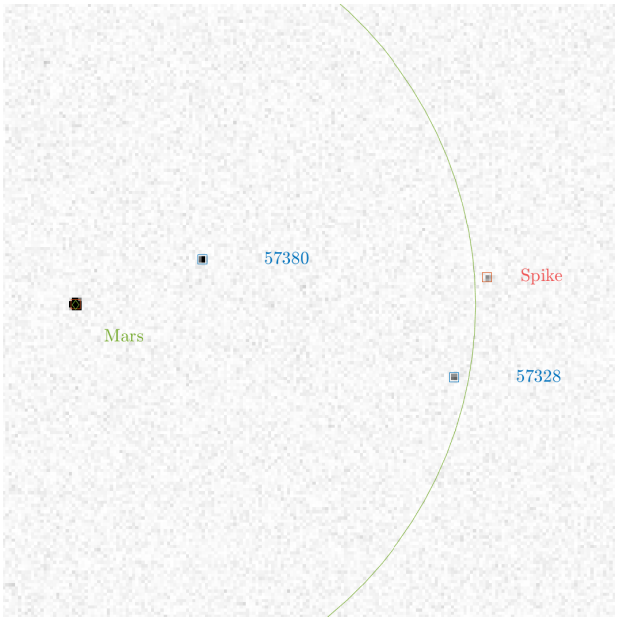

(d) Close-up of Fig. 3c to highlight the recognized planet

Figure 3. Steps of the IP pipeline. The centroids not recognized as stellar objects are labeled as spiked, whereas the stars are associated with their ID.

Filtering Strategy. The orbit determination algorithm chosen for the development of the autonomous navigation pipeline is selected by taking into account the limited computation capabilities of a CubeSat miniaturized processor. In particular, the chosen algorithm is a non-dimensionless EKF fed by planet position projections. The non-dimensionless EKF is proved in [14] to be an optimal choice for cutting down the computational effort and increasing the numerical stability of the filter. A position $\bar{r}$ and an epoch $\bar{t}$ parameter are exploited to non-dimensionalize the filtering procedure. The dimensionless state vector $\bar{\boldsymbol{x}}$ is defined as

$$\bar{\boldsymbol{x}} = \begin{bmatrix} \boldsymbol{r}/\bar{r} \\ \boldsymbol{v}/(\bar{r}\bar{t}^{-1}) \\ \boldsymbol{\eta}_{\mathrm{R}}/(\bar{r}\bar{t}^{-2}) \\ \boldsymbol{\eta}_{\mathrm{SRP}}/(\bar{r}\bar{t}^{-2}) \end{bmatrix} \tag{18}$$

and the same argument is applied for evaluating the dimensionless equation of motion $\bar{\boldsymbol{f}}$, the measurement model equation $\bar{\boldsymbol{h}}$, their associated Jacobian matrices $\bar{\boldsymbol{F}}$ and $\bar{\boldsymbol{H}}$, respectively, and the other covariance matrices $\bar{\boldsymbol{Q}}$, $\bar{\boldsymbol{R}}$ and $\bar{\boldsymbol{P}}_0$.

The filter scheme adopted in the VBN algorithm is reported in Tables 1, 2, and 3, where the state space, the propagation and the correction block are described, respectively. For sake of simplicity, the bar superscript is omitted. In the Tables hereunder, $\boldsymbol{x}_{p_k}$ represents the predicted state vector at epoch t_k with error covariance matrix $\boldsymbol{P}_{p_k}$, $\boldsymbol{K}_k$ is the Kalman gain, $\boldsymbol{x}_{c_k}$ is the corrected state vector with error covariance matrix $\boldsymbol{P}_{c_k}$, $\boldsymbol{r}_{\mathrm{pl_k}}$ is the observed beacon position, and $\boldsymbol{\nu}_k$ is the measurement error.

Table 1. System State Space

$\dot{\boldsymbol{x}} = \boldsymbol{f}(\boldsymbol{x}(t), t) + \boldsymbol{w}$
$\boldsymbol{r}_{\mathrm{pl_k}} = \boldsymbol{h}(\boldsymbol{x}_k) + \boldsymbol{\nu}_k$
$\dot{\boldsymbol{P}} = \boldsymbol{F}\boldsymbol{P} + \boldsymbol{P}\boldsymbol{F}^\top + \boldsymbol{Q}$

Table 2. Propagation Block

$\boldsymbol{x}_{p_k} = \boldsymbol{x}_{c_{k-1}} + \int_{t_{k-1}}^{t_k} \boldsymbol{f}(\boldsymbol{x}(t), t)\mathrm{d}t$
$\boldsymbol{x}_{c_0} = E[\boldsymbol{x}_0]$
$\boldsymbol{P}_{p_k} = \boldsymbol{P}_{c_{k-1}} + \int_{t_{k-1}}^{t_k} \dot{\boldsymbol{P}}\mathrm{d}t$
$\boldsymbol{P}_{c_0} = E[\boldsymbol{x}_0\boldsymbol{x}_0^\top]$

Table 3. Correction Block

$\boldsymbol{K}_k = \boldsymbol{P}_{p_k}\boldsymbol{H}_k^\top(\boldsymbol{H}_k\boldsymbol{P}_{p_k}\boldsymbol{H}_k^\top + \boldsymbol{R}_k)^{-1}$
$\boldsymbol{x}_{c_k} = \boldsymbol{x}_{p_k} + \boldsymbol{K}_k[\boldsymbol{r}_{\mathrm{pl_k}} - \boldsymbol{h}(\boldsymbol{x}_{p_k})]$
$\boldsymbol{P}_{c_k} = (\boldsymbol{I} - \boldsymbol{H}_k\boldsymbol{H}_k)\boldsymbol{P}_{p_k}(\boldsymbol{I} - \boldsymbol{K}_k\boldsymbol{H}_k)^\top + \boldsymbol{K}_k\boldsymbol{R}_k\boldsymbol{K}_k^\top$

Eventually, since large outliers can worsen the estimation, an online outlier rejection approach is introduced[28] in the filter correction block. When the absolute value of the innovation term ($||\boldsymbol{r}_{\mathrm{pl_k}} - \boldsymbol{h}(\boldsymbol{x}_{p_k})||$) is greater than a threshold, the innovation term is set to zero, and the correction of the propagated state estimation is not performed. It is, indeed, preferred to keep an old but good prediction to not worsen the estimation.

Results.

Navigation Strategy. The navigation algorithm is tested on an interplanetary trajectory leg between Earth and Mars. Starting from the initial time t_0, the spacecraft tracks the first planet of the optimal pair for 60 minutes. Then, it performs a slew maneuver of 30 minutes and, eventually, it observes the second planet for another hour. This navigation cycle is repeated every five days for a 50-days trajectory leg. Figure 4 shows the selected navigation cycle. At the beginning of each navigation leg,

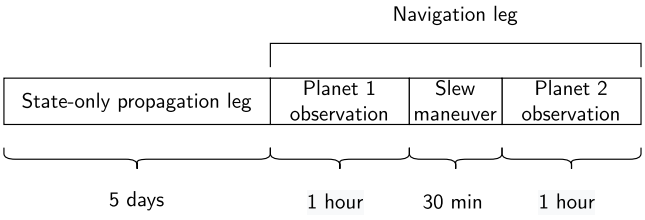

Figure 4. Navigation cycle

the optimal selection approach is adopted to determine which couple of planet is best to track to obtain the highest filter performances. The threshold values of the SEA and apparent magnitude considered to assess the planet visibility are 20 [deg] and 7, respectively. For the analyzed test case, the optimal selection method results in the selection of the pair Earth-Mars in each navigation leg.

Filter Settings. The initial probe position and velocity is selected by randomly sampling a Gaussian distribution centered in the probe nominal state and with $\sigma_r = 10^4$ km, $\sigma_v = 10^{-1}$ km/s, respectively. The probe initial state in the ecliptic J2000 reference frame is reported in Table 4. Instead, the uncertainties σ_{SRP}, σ_{R} and $\sigma_{\mathrm{c}_{\boldsymbol{r}_{\mathrm{pl}}}}$ to determine the error covariance matrices $\boldsymbol{P}_0$, $\boldsymbol{Q}$, and $\boldsymbol{R}$ are detailed in Table 5. Note that the matrix $\boldsymbol{R}$ is defined by taking into account in a conservative way the results of the Monte Carlo analysis performed in 18, which assesses the planet projection errors as a function of the probe position uncertainty.

Camera Settings. The onboard camera is assumed to have the characteristics reported in Table 6, where F is the f-number, $\mathrm{Q_e} \times \mathrm{T_{lens}}$ is the quantum efficiency ×

Table 4. Probe state at $t_0 = 9901$ ***mjd2000***

	$\boldsymbol{r}_0$ [km]	$\boldsymbol{v}_0$ [km/s]	$\boldsymbol{\eta}_0$ [km/s^2]
x-component	-1.28·10^8	-23.28	0
y-component	1.18·10^8	-13.46	0
z-component	5.40·10^7	-5.81	0

lens transmission, σ_d is the defocus level, and n_{CR} is the number of single pixels that are turned on for simulating the presence of hitting cosmic rays.

Filter Performances. The filter performances are studied through a Monte Carlo analysis conducted on 100 samples. Figures 5 and 6 show the position and velocity error profiles and covariance bounds over the trajectory leg considered in the J2000 ecliptic reference frame. Since both the planets and the spacecraft lie almost on the ecliptic plane, the x and y components represent the in-plane error, whereas z is the out-of-plane one. At the end of the trajectory leg, the filter estimates the spacecraft position and velocity with a 3σ accuracy of 1025 km and 0.42 m/s, respectively. The 3σ sample and filter covariance profiles are mostly overlapped, which suggests that the filter and its covariance matrices, in particular $\boldsymbol{R}$, are well tuned. Moreover, a comparison with the performances of the orbit determination algorithm described in 14 can be performed. By considering the same settings for the camera and navigation cycle, it is possible to notice that the orbit determination algorithm in 14 fed by the planet LoS directions reaches a higher accuracy in the estimation of the spacecraft state (about 900 km for the position). The reason is that the external observations have been modeled by considering a smaller 3σ error, equal to 15 arcsec, which is also adopted to build the measurement error covariance matrix $\boldsymbol{R}$. Instead, in this paper, the 3σ measurement error of the planet observation extracted from deep-space images is revealed to be greater than the past prediction. Indeed, the error is estimated to be about 0.3 px along both directions of the $\mathbb{C}$ camera frame, which means about 20 arcsec for a camera with FoV of 20 [deg] and sensor frame of dimension 1024 $\times$ 1024.

Moreover, the importance of the implementation of strategies for correcting the light-time and light-aberration effects is here demonstrated. Indeed, when these are not included, the performances of the autonomous deep-space navigation filter greatly degrade, and the error profiles do not converge to zero. In particular, Figure 7 displays the filter performances in the estimation of the position and velocity errors when the light effects are not corrected. The sample error profiles are biased, which reflect a modeling error in the measurement equation of the filter.

Conclusion. A vision-based navigation filter suited for deep-space CubeSats is developed in this paper. A dimensionless extended Kalman filter fed by planet position projections retrieved from deep-space images[18] is chosen to take into account the limited capabilities of a deep-space CubeSat processor. The IP pipeline exploited to extract the planet information from the generated image is described in 18, in which a correction step is added between attitude determination and planet identification to compensate for the light-aberration effect on stars centroids. Instead, for correcting the light-time and light-aberration effects affecting the planet position projection, the measurement model equation h is derived such that it represents the planet position projection at time τ and is shifted by the quantity defined by the light-aberration effect. In this way, the observation adopted to correct the prediction is not dependent on the estimation itself.

At the end of the analyzed trajectory leg between Earth and Mars, the filter estimates the spacecraft position and velocity with a 3σ accuracy of 1025 km and 0.42 m/s, respectively. Future analysis should test the performances of the IP pipeline for different working conditions, such as on orbits toward outer and inner planets, and by including the estimation of the probe attitude in the filter. Moreover, it has been noticed that the pair of planets selected as optimal by the optimal selection method that yields the highest accuracy in the state estimation is not generally optimal for the IP pipeline. Indeed, on one side, the optimal planet selection method prefers planets close to the spacecraft and with an angle γ near 90 [deg]. On the other side, the IP pipeline has a higher success rate when the planet is further from the spacecraft since the region where it could be detected would become more undersized, and a misidentification is less likely to occur.

Eventually, future analysis should test the performances of the IP pipeline during hardware-in-the-loop simulations. In this context, a camera acquires a sky-field image, rendered on a high-resolution screen, and gives the associated matrix of digital counts to the IP algorithm,[29] which retrieves the planet observation that feeds a VBN filter deployed on a processor representative of a CubeSat miniaturized onboard computer.[14]

Acknowledgments. This research is part of EXTREMA, a project that has received funding from the European Research Council (ERC) under the European Union's Horizon 2020 research and innovation programme (Grant Agreement No. 864697).

Table 5. Filter uncertainties of the process and measurement noise

σ_{SRP} $[km/s^2]$	σ_{R} $[km/s^2]$	$\sigma_{\mathbb{C}_{\boldsymbol{r}_{\mathrm{pl}}}}$ [px]
10^{-10}	10^{-10}	[0.1 0; 0 0.1]

Table 6. Onboard camera characteristics.

FoV [deg]	20
F [-]	2.2
T [ms]	400
Image size [px]	1024$\times$ 1024
f [mm]	40
$\mathrm{Q_e}\times$ $\mathrm{T_{lens}}$	0.49
σ_d [px]	0.9
n_{CR}	2

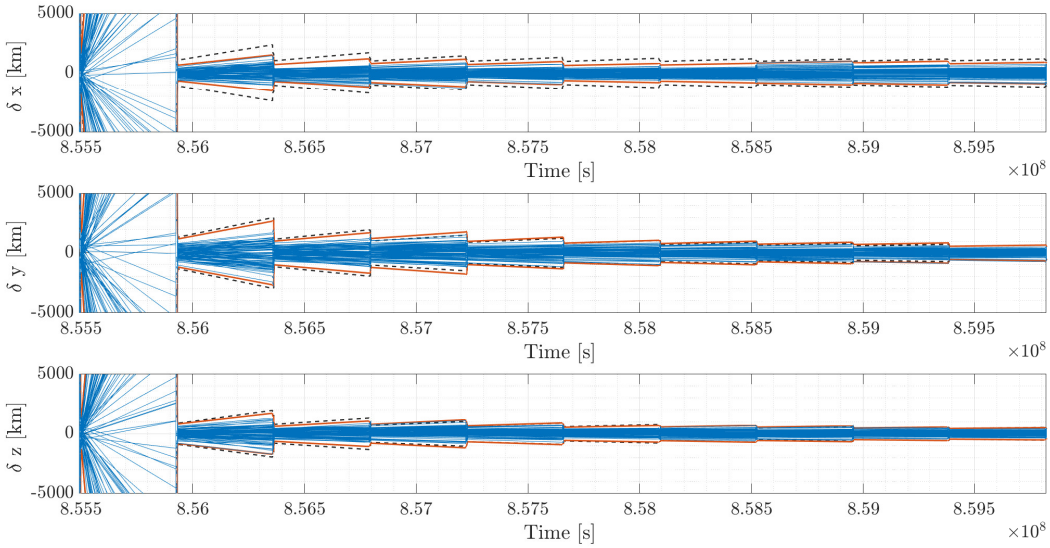

Figure 5. Position error profiles and covariance bounds when light effects are corrected in the filter. The sample error profiles are represented with blue solid lines, the 3σ filter covariance bounds with black dashed lines, and, the 3σ samples covariance bounds with orange solid lines. The x-axis represents the seconds since 01-01-2000, 12:00 noon.

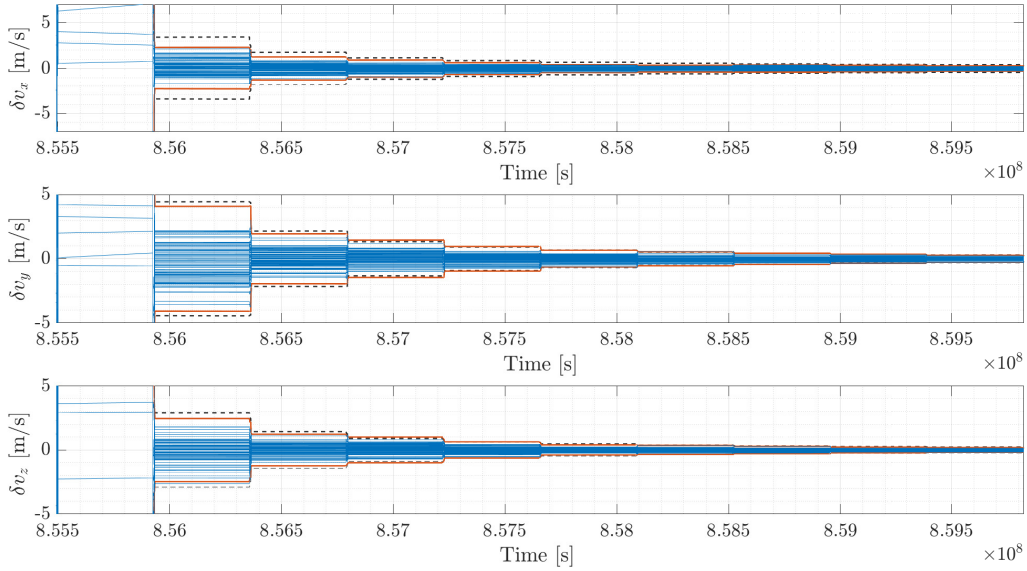

Figure 6. Velocity error profiles and covariance bounds when light effects are corrected in the filter. The sample error profiles are represented with blue solid lines, the 3σ filter covariance bounds with black dashed lines, and, the 3σ samples covariance bounds with orange solid lines. The x-axis represents the seconds since 01-01-2000, 12:00 noon.

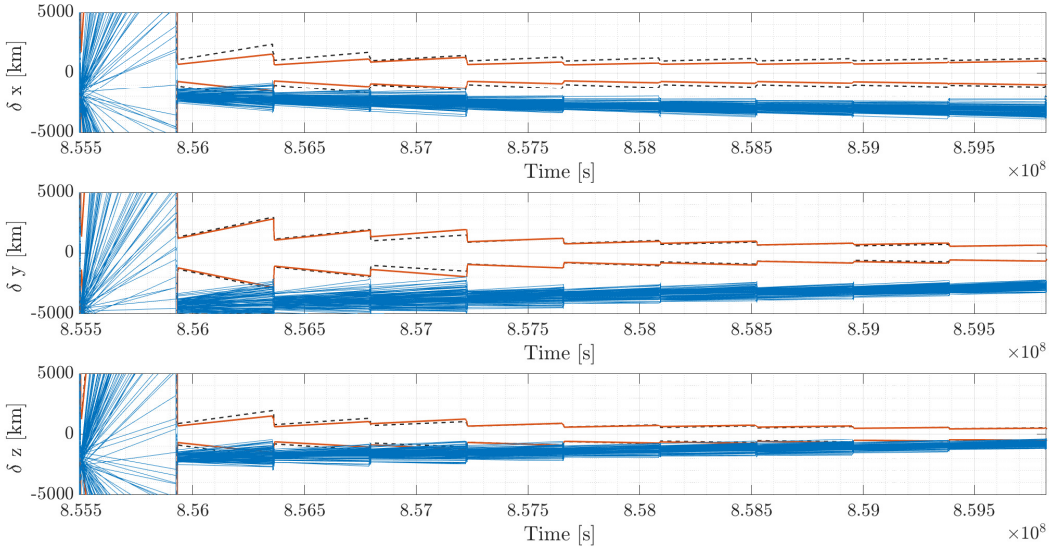

Figure 7. Position error profiles when light effects are not corrected in the filter. The sample error profiles are represented with blue solid lines, the 3σ filter covariance bounds with black dashed lines, and, the 3σ samples covariance bounds with orange solid lines. The x-axis represents the seconds since 01-01-2000, 12:00 noon.

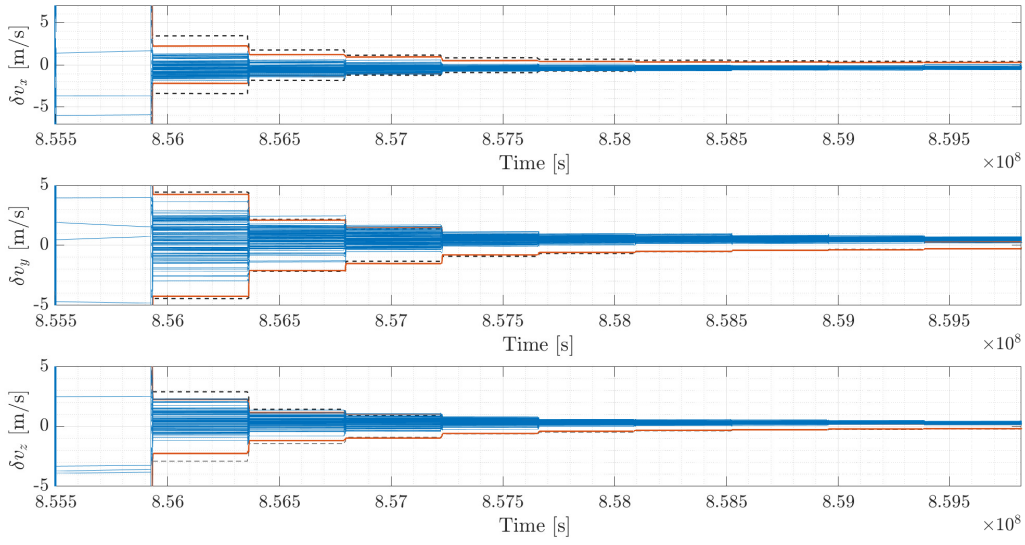

Figure 8. Velocity error profiles when light effects are not corrected in the filter. The sample error profiles are represented with blue solid lines, the 3σ filter covariance bounds with black dashed lines, and, the 3σ samples covariance bounds with orange solid lines. The x-axis represents the seconds since 01-01-2000, 12:00 noon.

References.

[1] T. Villela, C. Costa, A. Brandão, F. Bueno, and R. Leonardi, "Towards the thousandth cubesat: A statistical overview," *International Journal of Aerospace Engineering*, vol. 2019, 01 2019.

[2] R. Walker, D. Binns, C. Bramanti, M. Casasco, P. Concari, D. Izzo, D. Feili, P. Fernandez, J. Fernandez, P. Hager, D. Koschny, V. Pesquita, N. Wallace, I. Carnelli, M. Khan, M. Scoubeau, and D. Taubert, "Deep-space cubesats: Thinking inside the box," *Astronomy & Geophysics*, vol. 59, pp. 5.24–5.30, 10 2018.

[3] B. K. Malphrus, A. Freeman, R. Staehle, A. T. Klesh, and R. Walker, "4 - interplanetary cubesat missions," in *Cubesat Handbook* (C. Cappelletti, S. Battistini, and B. K. Malphrus, eds.), pp. 85–121, Academic Press, 2021.

[4] S. M. Lichten, D. S. Abraham, B. Arroyo, S. W. Asmar, J. Bell, and C. D. Edwards, "Allocation of deep space network ground system tracking and communications assets during the 2020-2021 timeframe of the "mars armada"," in *2018 SpaceOps Conference*, 2018.

[5] J. S. Border and C. L. Thornton, *Range and Doppler Tracking Observables*, ch. 3, pp. 9–46. John Wiley & Sons, Ltd, 2000.

[6] M. Xue, Y. Shi, Y. Guo, N. Huang, D. Peng, J. Luo, H. Shentu, and Z. Chen, "X-ray pulsar-based navigation considering spacecraft orbital motion and systematic biases," *Sensors*, vol. 19, no. 8, p. 1877, 2019.

[7] E. Turan, S. Speretta, and E. Gill, "Autonomous navigation for deep space small satellites: Scientific and technological advances," *Acta Astronautica*, vol. 193, pp. 56–74, 2022.

[8] S. Bhaskaran, "Autonomous navigation for deep space missions," in *SpaceOps 2012*, p. 1267135, 2012.

[9] S. Henry and J. A. Christian, "Absolute triangulation algorithms for space exploration," *Journal of Guidance, Control, and Dynamics*, vol. 0, no. 0, pp. 1–26, 0.

[10] R. Karimi and D. Mortari, "Interplanetary autonomous navigation using visible planets," *Journal of Guidance, Control, and Dynamics*, vol. 38, pp. 1–6, 04 2015.

[11] V. Franzese, *Autonomous Navigation for Interplanetary CubeSats at different scales*. PhD thesis, Milan, Italy, Politecnico di Milano, 2021.

[12] A. Giannitrapani, N. Ceccarelli, F. Scortecci, and A. Garulli, "Comparison of ekf and ukf for spacecraft localization via angle measurements," *IEEE Transactions on Aerospace and Electronic Systems*, vol. 47, no. 1, pp. 75–84, 2011.

[13] V. Franzese, F. Topputo, F. Ankersen, and R. Walker, "Deep-space optical navigation for m-argo mission," *The Journal of the Astronautical Sciences*, vol. 68, no. 4, pp. 1034–1055, 2021.

[14] E. Andreis, V. Franzese, and F. Topputo, "Onboard orbit determination for deep-space cubesats," *Journal of Guidance, Control, and Dynamics*, pp. 1–14, 2022.

[15] J. A. Christian, "Optical navigation using planet's centroid and apparent diameter in image," *Journal of guidance, control, and dynamics*, vol. 38, no. 2, pp. 192–204, 2015.

[16] P. Panicucci, *Autonomous vision-based navigation and shape reconstruction of an unknown asteroid during approach phase*. PhD thesis, Toulouse, France, Institut Supérieur de l'Aéronautique et de l'Espace, 2021.

[17] V. Franzese, P. Di Lizia, and F. Topputo, "Autonomous optical navigation for the lunar meteoroid impacts observer," *Journal of Guidance, Control, and Dynamics*, vol. 42, no. 7, pp. 1579–1586, 2019.

[18] E. Andreis, P. Panicucci, V. Franzese, and F. Topputo, "A robust image processing pipeline for planets line-of-sign extraction for deep-space autonomous cubesats navigation," in *44th AAS Guidance, Navigation and Control Conference*, pp. 1–19, 2022.

[19] J. Riedel, S. Bhaskaran, S. Desai, D. Han, B. Kennedy, T. McElrath, G. Null, M. Ryne, S. Synnott, T. Wang, *et al.*, "Using autonomous navigation for interplanetary missions: The validation of deep space 1 autonav," 2000.

[20] G. D. Domenico, E. Andreis, A. C. Morelli, G. Merisio, V. Franzese, C. Giordano, A. Morselli, P. P. F. Ferrari, and F. Topputo, "Toward self-driving interplanetary cubesats: The erc-funded project extrema," in *72nd International Astronautical Congress*, 10 2021.

[21] S. Henry and J. A. Christian, "Absolute triangulation algorithms for space exploration," *Journal of Guidance, Control, and Dynamics*, vol. 0, no. 0, pp. 1–26, 0.

[22] S. A. Bella, E. Andreis, V. Franzese, P.Panicucci, and F. Topputo, "Line-of-sight extraction algorithm for deep-space autonomous navigation," in *2021 AAS/AIAA Astrodynamics Specialist Conference*, 08 2021.

[23] V. Franzese and F. Topputo, "Optimal beacons selection for deep-space optical navigation," *The Journal of the Astronautical Sciences*, 11 2020.

[24] I. Jean, A. Ng, and A. K. Misra, "Impact of solar radiation pressure modeling on orbital dynamics in the vicinity of binary asteroids," *Acta Astronautica*, vol. 165, pp. 167–183, 2019.

[25] C. N. D. J. R. Carpenter, "Navigation Filter Best Practices," Tech. Rep. 20180003657, NASA, 04 2018.

[26] D. Mortari, "Search-less algorithm for star pattern recognition," *Journal of the Astronautical Sciences*, vol. 45, 04 1997.

[27] F. L. Markley and J. L. Crassidis, *Fundamentals of spacecraft attitude determination and control*, ch. 3 Static Attitude Determination Methods, pp. 183–235. Springer, 2014.

[28] H. Liu, S. Shah, and W. Jiang, "On-line outlier detection and data cleaning," *Computers & chemical engineering*, vol. 28, no. 9, pp. 1635–1647, 2004.

[29] P. Panicucci, M. Pugliatti, V. Franzese, and F. Topputo, "Improvements and applications of the dart vision-based navigation test-bench tinyv3rse," in *AAS GN&C conference*, Breckenridge, CO, U.S.A., 3 - 9 February 2022.